Integrated Simulation and State Estimation for Precision Landing on Titan

Aaron Schutte, Jeff Delaune, Evgeniy Skylanskiy, Robert Hewitt, Shreyansh Daftry, Marco B. Quadrelli and Larry Matthies
Jet Propulsion Laboratory
California Institute of Technology
4800 Oak Grove Dr.
Pasadena, CA 91109

***Abstract*—This paper reports on a study of the application of a ram-air parafoil to Entry, Descent, and Landing (EDL) on Titan. A comprehensive simulation was constructed to enable simulation of EDL state estimation performance from 10 minutes before entry (E-10 min) to touchdown on the surface of Titan. EDL performance is characterized assuming an entry phase starting at E-10 min followed by a parafoil guided phase for descent and landing to enable precise landing on a predetermined target. Guided descent during the parafoil phase is achieved using the parafoil steering capability while state estimation is accomplished using vision-based Terrain Relative Navigation (TRN). The simulation is used in this study to conduct Monte Carlo analysis of TRN state estimation for a full entry phase sequence followed by a straight line flight path descent and landing.**

TABLE OF CONTENTS

1. INTRODUCTION.....2
2. MISSION DESIGN AND EDL ARCHITECTURE 2
3. END-TO-END SIMULATION.....3
4. TRN STATE ESTIMATION 8
5. MONTE CARLO SIMULATION RESULTS.....9
6. SUMMARY AND FUTURE WORK..... 11
REFERENCES 12
BIOGRAPHY 13

1. INTRODUCTION

Titan is a complex, diverse Ocean World that will require multiple missions to understand it's organic chemistry and potential habitability. Landing dispersions with existing technology are hundreds of kilometers wide, which could place future landers far from the most scientifically promising terrain. The objective of this work is to address the problems of and investigate appropriate solutions to Guidance & Control aspects of autonomous Precision Aerial Delivery Systems for payload delivery using parafoils on Titan. As part of this effort, and leveraging past work [1–4], we have been developing a simulation of end-to-end EDL (Entry, Descent, and Landing) performance and using the simulation to estimate and optimize expected landing dispersion, with the goal of showing feasibility of reducing delivery error by at least 100 km compared to Huygens-like descent.

We have extended our in-house Dynamics Simulator for Entry, Descent and Landing (DSENDS) [5] with libraries of vehicle dynamics models to handle the parafoil concept proposed here and the specific state estimation, tracking, and control capability in conditions relevant to Titan's environment. Terrain Relative Navigation (TRN) estimation is based on an Extended Kalman Filter - Simultaneous Localization and Mapping (EKF-SLAM) algorithm and is a key component in this study for determining lander delivery error [6]. For simulation purposes, the TRN estimation [7] is carried out independently from the DSENDS simulation over a Robot Operating System (ROS) node. We have developed and tested several dynamic models of the parafoil system descending in Titan's atmosphere based on models previously used for simulation in the Martian environment [2], and we have expanded these dynamic models to enable higher fidelity descent simulations to assess the impact on the landing precision. A six degrees of freedom capsule and parafoil system model has been implemented to efficiently simulate the desired conditions for the entry, descent, and landing phases.

In the following, we describe (1) a Titan relevant mission design and EDL architecture, (2) the integrated end-to-end simulation used to evaluate TRN state estimation performance, (3) the proposed TRN state estimation framework, and (4) the results of a TRN state estimation Monte Carlo analysis of an E-10 min to ground EDL sequence using a Maracaibo Lacus scenario.

2. MISSION DESIGN AND EDL ARCHITECTURE

Mission Design and Navigation (MDNAV)

An overall architecture for Titan EDL is highly coupled to a mission design scenario and a corresponding approach navigation for a particular interplanetary trajectory. The Earth launch opportunity was chosen based on the approximate time frame of New Frontiers 5. The Earth-Earth Jupiter Saturn (EEJS) interplanetary trajectory was designed with a launch date on 1 Nov 2035 and a Saturn system arrival in May-Dec of 2046. A 10.6 year transfer assumes Earth and Jupiter gravity assisted flybys as well as a deep space maneuver of 860 m/s. The interplanetary trajectory had to be linked with each EDL scenario for a chosen landing site analyzed in this study. A Titan direct entry and an atmospheric entry from Saturn's elliptical orbit are the two main approach trajectory cases analyzed for Titan landing site analysis. The direct entry case is analogous to most of the Mars EDL missions, where the entry probe/vehicle is separated from the spacecraft cruise at E-10 min. This approach allows to minimize the navigation delivery and knowledge position/velocity errors that are critical for EDL. The second trajectory scenario is similar to Huygens EDL, where the probe is released (E-7 days) from the spacecraft, which is in an elliptical orbit around Saturn. Titan is locked in

©2019 California Institute of Technology. Government sponsorship acknowledged. This research was carried out at the Jet Propulsion Laboratory, California Institute of Technology, under a contract with the National Aeronautics and Space Administration.

Authorized licensed use limited to: Jet Propulsion Laboratory. Downloaded on November 18,2024 at 21:16:46 UTC from IEEE Xplore. Restrictions apply.

Saturn's orbital rotation which makes the MDNAV problem overly constrained during the targeting process, especially for the Titan direct interplanetary trajectories. The two reference landing sites such as Huygens probe (10.25° S, 192.32° W) and Maracaibo Lacus interlake region (74.95° N, 128.67° W) have been chosen to fully investigate the MDNAV/EDL feasibility. The northern Maracaibo landing site for Titan's direct entry requires a shallow Entry Flight Path Angle (EFPA) of -51° whereas the Huygens site can be targeted with EFPA of -65°. A Titan entry from Saturn's orbit can be achieved with steeper EFPA of -71° at the expense of the increased EFPA uncertainty as well as position knowledge error. Figure 1 illustrates parametric trades of the MDNAV/landing sites which can have a direct impact on EDL performance. A Huygens type of entry vehicle was used in EDL trajectory analysis for the cases summarized in the figure.

EDL Architecture

The EDL architecture will primarily be driven by the lander design and packaging constraints within the aeroshell. In this study the entry probe mass was chosen to be 320 kg to make a compelling comparison case with Huygens mission. For the EDL mechanical configuration, the capsule diameter was constrained to 2 m. The two aeroshell configurations were analysed in this study assuming 60° and 45° heatshield geometries. The 60° spherecone case is based on the Huygens style EDL Concept of Operations (ConOps) where the probe releases a small drogue parachute at approximately Mach 1.5 in order to mitigate the capsule instabilities during the transonic phase. For a given probe mass, this is typically achieved at 135 km above the surface of Titan. Another approach for a conceptual entry vehicle is to use the Pioneer Venus Large Probe heritage for a 45° spherecone geometry. Figure 2 illustrates the geometry and the mass properties of the Pioneer Venus Large Probe mechanical design which were used as a reference in this study for the mass/inertia scaling laws. A 45° spherecone entry probe allows a more aggressive scenario where the probe would fly through the transonic phase without the need to deploy the stabilizing drogue chute. This particular approach can reduce the EDL timeline, minimize the wind drift on the parachute and reduce the overall footprint size. The outlined concept was chosen as a baseline for this study and the development of the EDL end-to-end simulation. The ConOps was constructed based on the Titan Direct hyperbolic trajectory for the Maracibo Lacus site with EFPA of -51° at 1500 km entry interface altitude. Figures 3 and 4 illustrate the key EDL events and an overall timeline for a baseline case used in the end-to-end EDL simulation. As can be seen from the figure, shortly after the atmospheric entry (E+3.8 min) the probe will experience the heat pulse and the peak deceleration at E+4 min. The capsule then would fly through the transonic phase without losing dynamic stability and the main chute would be deployed at E+30 min. The main objective of the main chute is to create a necessary ballistic coefficient ratio for a successful heatshield release. Once the heatshield is released at 40 km altitude Above Ground Level (AGL), the altimeter starts the ground acquisition. After the altitude solution is acquired the EDL sequences transitions into TRN with lander vision map matching technique. At E+32 min after entry the main chute is jettison followed by the parafoil deployment. The aeromaneuvering would continue for approximately 3 hours after deployment in preparation for the final approach and landing phase. The technical details of the parafoil modeling within the EDL simulation are described in the subsequent sections.

3. END-TO-END SIMULATION

The Guidance & Control simulation architecture is based on the DSENDS multi-mission framework [8]. The simulation is designed to simulate EDL performance from capsule entry conditions at E-10 min to touchdown on Titan. Figure 5 illustrates the primary components included in the simulation.

Titan Environment

The simulation uses the Global Reference Atmospheric Model (GRAM) Titan-GRAM 2004 by default for modeling Titan atmospheric density and winds. Compared to Earth and Mars, Figure 6 illustrates Titan's significantly more dense atmosphere (4x more dense than Earth at the surface). At the surface, the Yelle model [9]

$$\rho = 5.43 \exp\left(\frac{-0.0512h}{1000}\right) \tag{1}$$

and Titan-GRAM 2004 are comparable, but begin to differ at altitudes h greater than 40 km. Titan zonal winds (East-West) are much larger than meridional (North-South) winds except near the poles where upper bound wind speeds reach approximately $1\ \mathrm{m/s}$ over a Saturn year [10].

Although Titan is larger than the Moon, Titan's gravity $g = 1.35\ \mathrm{m/s^2}$ at the surface is smaller due to its lower density. The simulation implements a general N–body gravity model that includes planetary ephemeris obtained using the Navigation Ancillary Information Facility (NAIF) SPICE DE430 and SAT375 libraries [11]. The default gravity model includes point mass gravitational acceleration effects from Saturn, Titan, Dione, Rhea, Iapetus, and the Sun.

Capsule and Parafoil Dynamics

During the entry phase the capsule dynamics are modeled using a six degree-of-freedom (6DOF) rigid body. The nominal capsule mass properties are listed in Table 1. The

Table 1. Capsule Mass Properties

Parameter	Value
mass	320 kg
inertia	$\begin{bmatrix} 71.9 & 0.45 & -0.096 \\ 0.45 & 75.85 & 0.338 \\ -0.096 & 0.338 & 127.97 \end{bmatrix}$ kg · m^2
center of mass	$\begin{bmatrix} 0 & 0 & 0 \end{bmatrix}$ m

DSENDS viewport in Figure 7 depicts the capsule during an entry phase scenario. 6DOF capsule aerodynamics and drogue parachute drag forces are included in the capsule dynamics model. 6DOF capsule aerodynamics are incorporated in the simulation for a 45° spherecone aeroshell using a lookup table database. The drogue parachute drag force on the capsule is modeled by applying a force in the opposite direction of the atmosphere relative velocity $\boldsymbol{v}_{rel}$ vector as

$$\boldsymbol{F}_p = -\frac{1}{2}\rho\|\boldsymbol{v}_{rel}\|C_{D_p}A_p\boldsymbol{v}_{rel}, \tag{2}$$

where C_{D_p} is the parachute drag coefficient and A_p is the parachute reference area.

The parafoil system is composed of (1) a rigid canopy airfoil body and (2) a rigid payload body that is attached to the

Authorized licensed use limited to: Jet Propulsion Laboratory. Downloaded on November 18,2024 at 21:16:46 UTC from IEEE Xplore. Restrictions apply.

EDL Mission Scenarios	Titan Direct Entry	Titan Direct Entry	Titan Entry from Saturn's Orbit
Titan Arrival	May 31, 2046 (Ls: 147 deg)	May 28, 2046 (Ls: 145.5 deg)	Dec 8, 2046 (Ls: 89.8 deg)
Entry V∞/Ventry	8.7 km/s (Saturn V∞ 2.94 km/s)	7.5 km/s	4.89 km/s(Saturn V∞ 3.42 km/s)
Entry Flight Path Angle	-51 deg (3σ:±9.28e-3)	-65 deg (3σ:±3.65e-2)	-71 deg (3σ:±0.51)
Entry Pos. Delivery Ellipse(3σ)	6.3km X 1.24km	9.6km X 4.27km	20.6kmX13.7km
Entry Pos. Knowledge Error(3σ)	3.0 km	1.0 km	9.0 km
Entry Peak G-load	15 g	19.5 g	7.5 g
Delivery Ellipse(3σ) @ 40km AGL	200.5km X 84.9km	217.6km X 23.8km	278.9km X 75.8km
Landing Site	Maraciabo Lacus 74. 95° N, 128.67° W	Huygens Site 10.45° S, 192.45°W	Maraciabo Lacus 74. 95° N, 128.67° W

Figure 1. Approach navigation and landing sites.

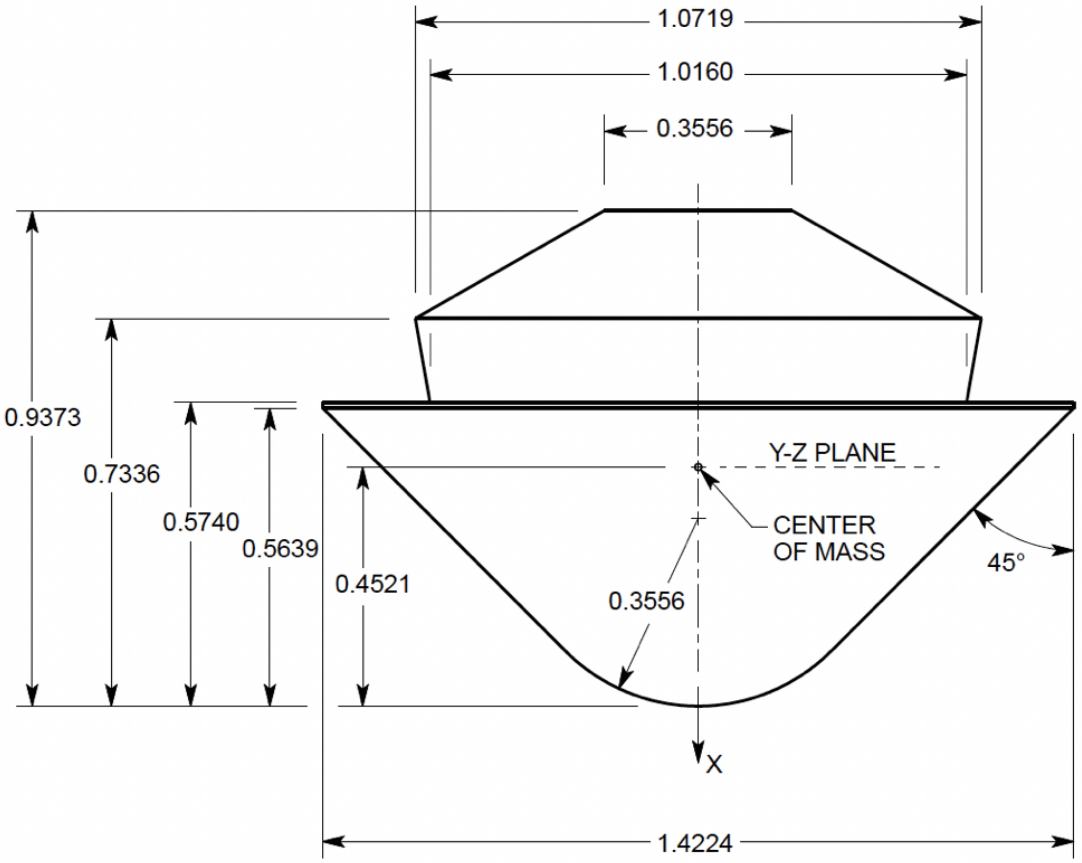

Description	Mass, m (kg)	x_{CoM}/D (from nose)	I_{xx} (kg•m^2) (roll)	I_{yy} (kg•m^2) (pitch)	I_{zz} (kg•m^2) (yaw)
Prior to entry	299.56	0.3178	44.2	32.9	29.6
After entry	292.16	0.3178	41.9	31.7	28.3

Figure 2. Pioneer Venus heritage mass properties.

Authorized licensed use limited to: Jet Propulsion Laboratory. Downloaded on November 18,2024 at 21:16:46 UTC from IEEE Xplore. Restrictions apply.

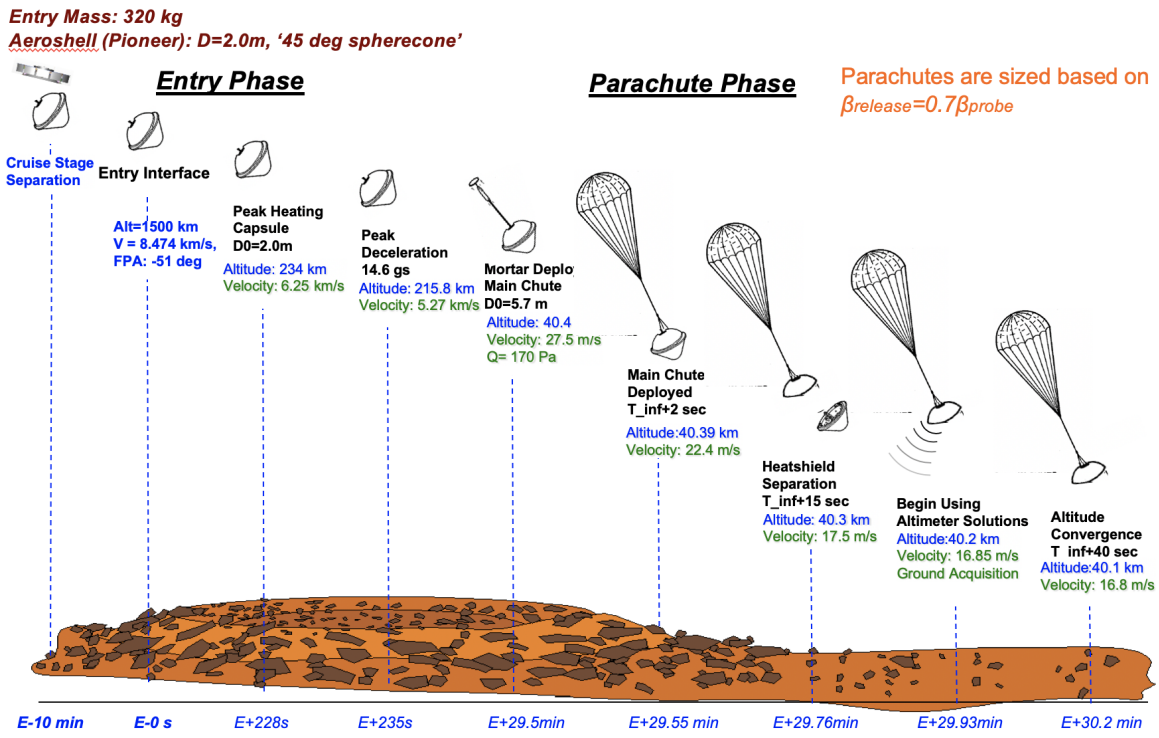

Figure 3. Titan EDL baseline ConOps from E-10 min to E+30.2 min

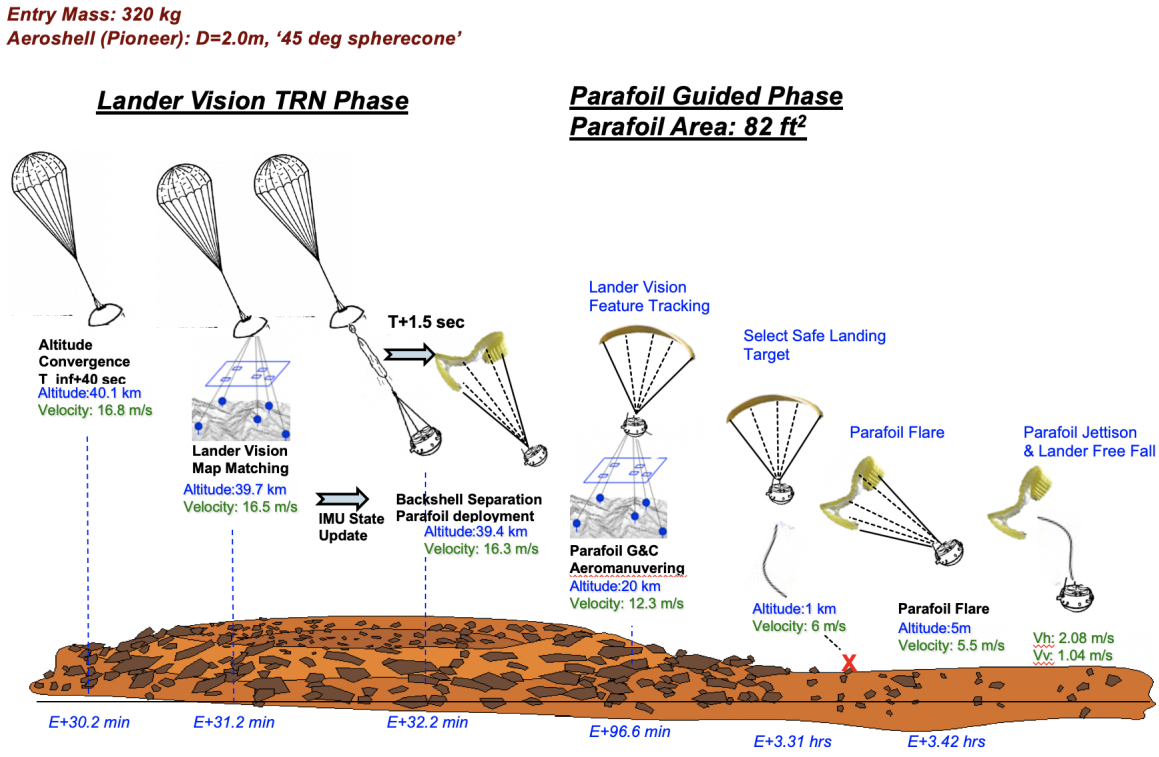

Figure 4. Titan EDL baseline ConOps from E+30.2 min to touchdown

Authorized licensed use limited to: Jet Propulsion Laboratory. Downloaded on November 18,2024 at 21:16:46 UTC from IEEE Xplore. Restrictions apply.

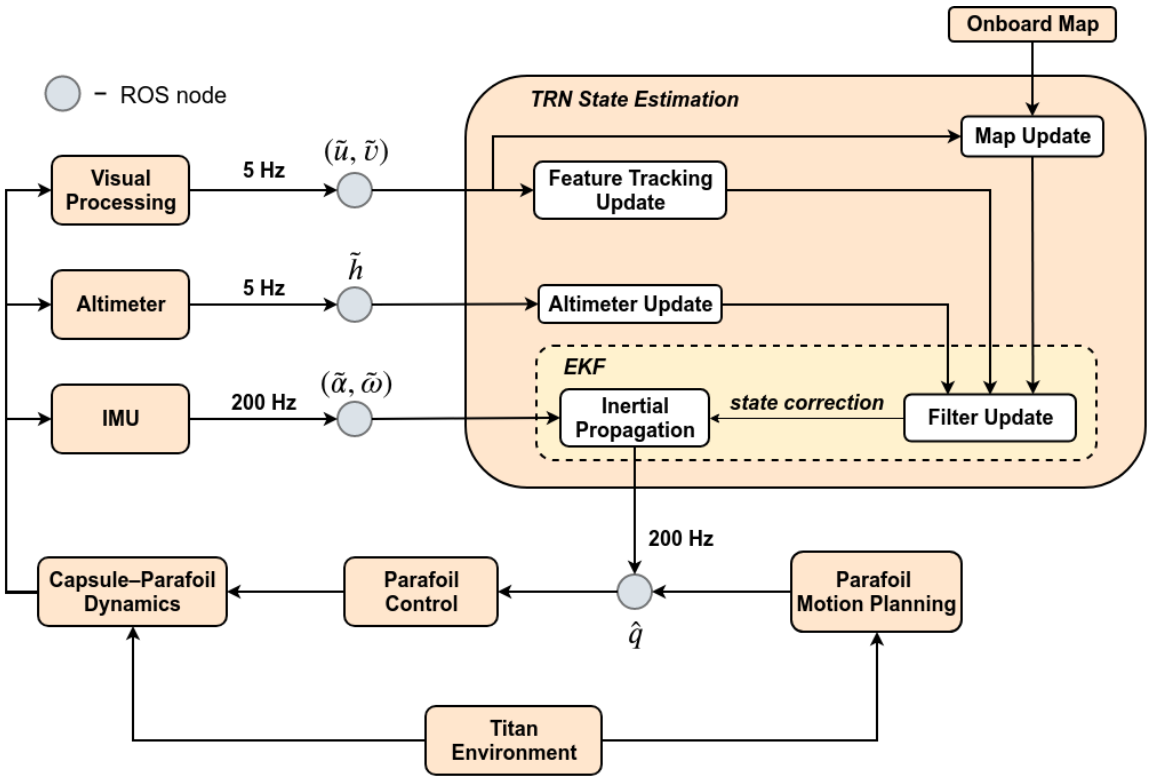

Figure 5. **DSENDS simulation and state estimation block diagram.**

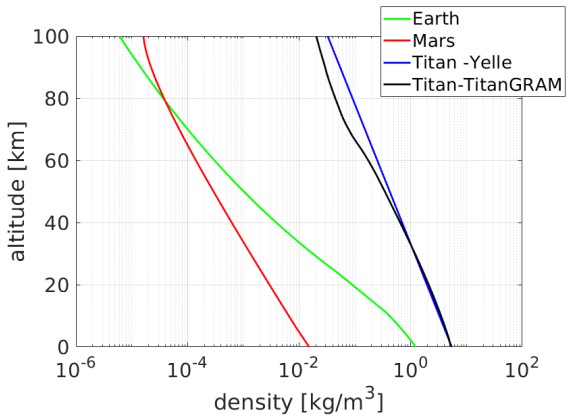

Figure 6. **Atmospheric density comparison.**

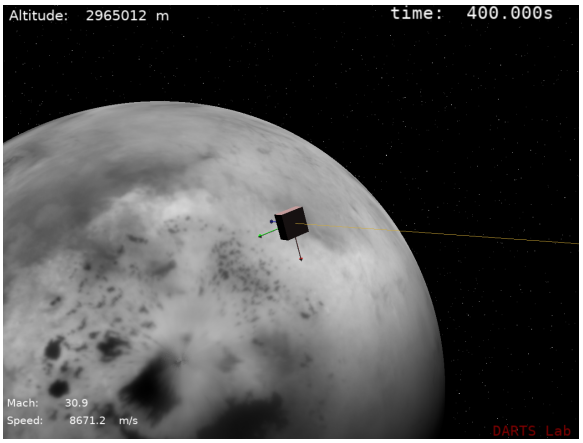

Figure 7. **DSENDS entry phase visualization.**

canopy using suspension lines. It is used during the descent phase in order to realize a guided system. The parafoil is able to actuate longitudinal and lateral dynamics by symmetrically and asymmetrically deflecting the parafoil flap, respectively. This enables turning, flaring, and velocity control of the vehicle. We have developed several dynamics models of the parafoil system that include point mass models (3 and 4 DOF) and rigid body models (6, 7, 8 and 9 DOF) that include relative dynamics between the canopy and payload bodies. The default simulation configuration uses the 6DOF model, which assumes the canopy is fully inflated with no deformation or relative motion between the canopy and the payload. Parafoil deployment is modeled such that the canopy is inflated instantaneously at the deployment event. The details of the parafoil 6DOF model, the aerodynamics coefficients used to model the aerodynamics forces acting on the parafoil, and the apparent mass and inertia effects are described in more detail in [2]. Figure 8 illustrates the canopy and payload coordinate systems during descent. The red, green, and blue axes correspond to the typical roll, pitch, and yaw angular motions.

Sensor Modeling

State estimation performance depends critically on an inertial measurement unit (IMU), two descent cameras [15], and an altimeter.

IMU—The IMU measurement model includes error modeling for individual gyroscope and accelerometer sensors; i.e., error models are specified for each gyroscope and accelerometer axis. This includes angle random walk (ARW), velocity

Authorized licensed use limited to: Jet Propulsion Laboratory. Downloaded on November 18,2024 at 21:16:46 UTC from IEEE Xplore. Restrictions apply.

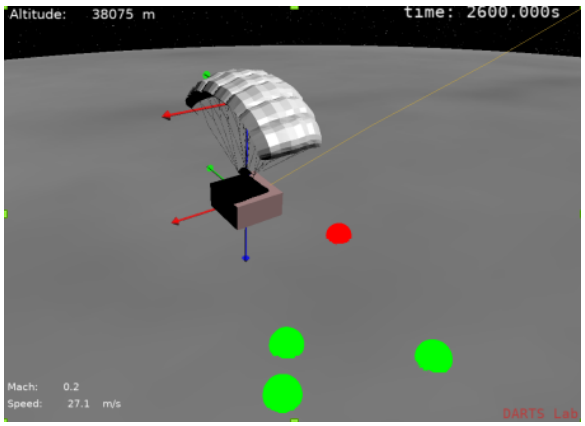

Figure 8. DSENDS descent phase visualization.

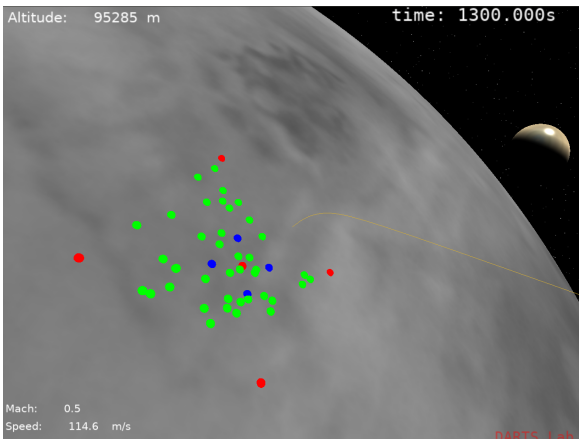

Figure 9. DSENDS feature map visualization.

random walk (VRW), scale factor error, constant rate bias, constant acceleration bias, misalignment, and quantization effects. We assume the IMU has three orthogonally mounted gyroscope sensors and three orthgonally mounted accelerometer sensors. Tables 2 and 3 list the 1-σ errors used in this study. These error parameters are consistent with a navigation grade Miniature Inertial Measurement Unit (MIMU).

Table 2. Gyro Error Parameters

Parameter	1-σ
ARW	0.01 deg/hr$^{0.5}$
scale factor	33.3 ppm
constant rate bias	0.3 deg/hr
misalignment	18 arcsec
quantization	1.8 μrad

Table 3. Accelerometer Error Parameters

Parameter	1-σ
VRW	0.033 m/s/hr$^{0.5}$
scale factor	150 ppm
constant accel bias	100 μg
misalignment	18 arcsec
quantization	2.7 mm/s

Visual processing— During the descent phase, a camera is used to accomplish visual-inertial odometry (VIO). We assume the camera has a 90° field-of-view (FOV) and is mounted at the bottom of the payload such that $\boldsymbol{d}_{camera} = [0, 0, 0.5]$ m relative to the payload frame. The camera simulation model is idealized to generate a buffer of features that intersect the camera focal plane and the surface of Titan. Figure 9 illustrates a snapshot of the available features in the FOV of the camera during descent. The five red sphere features are used for reference. They represent the line-of-sight (LOS) and the four corners of a 90° FOV camera. The four blue sphere features are used for map matching, which will be discussed in the following section. They are fixed in the camera frame at 20° from the LOS. Finally, the green sphere features are used for feature tracking, which will also be discussed in more detail in the following section. They are randomly generated features in the FOV. The camera model has a fixed-size buffer that is selected at runtime. When a feature leaves the FOV the camera model will randomly generate a new feature in the FOV to maintain the fixed-size buffer.

We assume Titan is spherically shaped in order to generate a feature on the surface. Under this assumption, the mapped feature coordinates in the Planet-Centered Inertial $\{PCI\}$ frame are obtained analytically by solving the quadratic equation

$$x^2 - 2\|\boldsymbol{p}_{PCI}^{c_i}\|(\hat{\boldsymbol{u}}_m \cdot \hat{\boldsymbol{n}}_T)x + \|\boldsymbol{p}_{PCI}^{c_i}\|^2 - r_{TITAN}^2 = 0, \quad (3)$$

where $\boldsymbol{p}_{PCI}^{c_i}$ is the position vector of the camera frame in the $\{PCI\}$ frame, $\hat{\boldsymbol{u}}_m$ is the unit vector from the camera frame to the feature, $\hat{\boldsymbol{n}}_T$ is the unit nadir vector, and r_{TITAN} is the mean Titan radius. The feature position in the $\{PCI\}$ frame is then

$$\boldsymbol{p}_m = \boldsymbol{p}_{PCI}^{c_i} + (\|\boldsymbol{p}_{PCI}^{c_i}\| - x)\,\hat{\boldsymbol{u}}_m. \quad (4)$$

Using the tracked feature position, the camera measurement model produces normalized image space coordinates

$$(\tilde{u}, \tilde{v}, 0) = \frac{1}{\hat{\boldsymbol{u}}_m \cdot \hat{\boldsymbol{u}}_{LOS}}\hat{\boldsymbol{u}}_m - \hat{\boldsymbol{u}}_{LOS} + \boldsymbol{n}_c, \quad (5)$$

where we assume $\hat{\boldsymbol{u}}_{LOS} = [0, 0, 1]$ is the LOS unit vector in the camera frame and $\boldsymbol{n}_c$ is zero-mean Gaussian white measurement noise. Camera measurement error modeling is split into map matching and feature tracking specific noise models in normalized image space coordinates. The noise models depend on Titan location specific imagery and are discussed in more detail in [15]. For the Maracaibo Lacus region, we use the 1-σ errors shown in Figures 10 and 11.

Altimeter—We assumed availability of direct altitude measurements through the following model

$${}^i z_h = \|\boldsymbol{p}_{PCI}^i\| - r_{TITAN} + n_h \quad (6)$$

where $\|\boldsymbol{p}_{PCI}^i\|$ is the Euclidean norm of the IMU position in $\{PCI\}$ and n_h is a zero-mean Gaussian white measurement noise. This is equivalent to nadir terrain radar measurement over a spherical Titan surface model. Future work should vary terrain range measurements as a function of spacecraft's attitude, and non-spherical surface model, but was considered beyond the scope of this project at first order. The 3-σ value of the standard deviation of $\boldsymbol{n}_h$ was set to 5% of ${}^i z_h$, to match the maximum error specification of Huygens' radar altimeter reported in [16].

Authorized licensed use limited to: Jet Propulsion Laboratory. Downloaded on November 18,2024 at 21:16:46 UTC from IEEE Xplore. Restrictions apply.

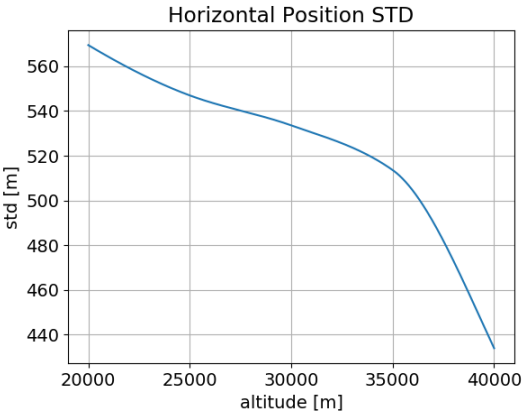

Figure 10. Map matching measurement uncertainty for the Maracaibo Lacus region.

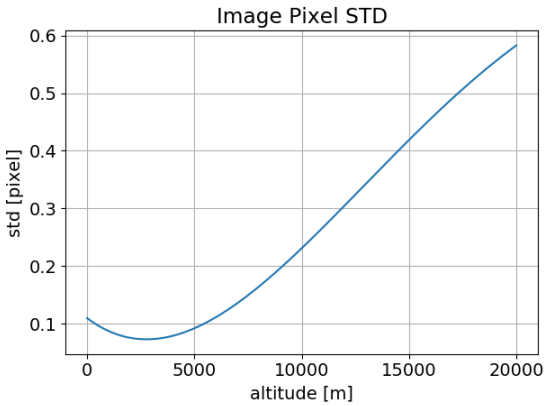

Figure 11. Feature tracking measurement uncertainty for the Maracaibo Lacus region.

4. TRN State Estimation

We estimate the state of the descent module using sensor inputs from vision, altimetry and IMU. Vision can provide image matching with respect to an orbital map, or frame-to-frame tracks of unmapped terrain features. Our state estimation architecture is illustrated in the upper right corner of Figure 5. It is based on an Extended Kalman filter. This section describes the inertial propagation, as well as the various sensor update models.

Inertial Propagation

Our state vector can be broken down into two components $\boldsymbol{x} = \begin{bmatrix} \boldsymbol{x}_I{}^T & \boldsymbol{x}_V{}^T \end{bmatrix}^T$. We will refer to $\boldsymbol{x}_I$ as inertial states, and $\boldsymbol{x}_V$ as vision states. The inertial states

$$\boldsymbol{x}_I = \begin{bmatrix} \boldsymbol{p}^i_{PCI}{}^T & \boldsymbol{v}^i_{PCI}{}^T & \boldsymbol{q}^i_{PCI}{}^T & \boldsymbol{b}_g{}^T & \boldsymbol{b}_a{}^T \end{bmatrix}^T \tag{7}$$

include the position, velocity and orientation of the IMU frame $\{i\}$ with respect to the $\{PCI\}$ frame, the gyroscope biases $\boldsymbol{b}_g$ and the accelerometer biases $\boldsymbol{b}_a$. Unit quaternions are used to model orientations.

Our system dynamics are time-varying and use the IMU measurements

$$\begin{cases} \dot{\boldsymbol{p}}^i_{PCI} &= \boldsymbol{v}^i_{PCI} \\ \dot{\boldsymbol{v}}^i_{PCI} &= \boldsymbol{C}(\boldsymbol{q}^i_{PCI})^T(\boldsymbol{a}_{IMU} - \boldsymbol{b}_a - \boldsymbol{n}_a) + {}^{PCI}\boldsymbol{g} \\ \dot{\boldsymbol{q}}^i_{PCI} &= \frac{1}{2}\boldsymbol{\Omega}(\boldsymbol{\omega}_{IMU} - \boldsymbol{b}_g - \boldsymbol{n}_g)\boldsymbol{q}^i_{PCI} \\ \dot{\boldsymbol{b}}_g &= \boldsymbol{n}_{b_g} \\ \dot{\boldsymbol{b}}_a &= \boldsymbol{n}_{b_a} \end{cases} \tag{8}$$

where $\boldsymbol{n}_\star$ are zero-mean Gaussian white random noise representing the IMU measurement noise and bias random walk. $\boldsymbol{C}(\boldsymbol{q})$ denotes the coordinate change matrix associated to a unit quaternion $\boldsymbol{q}$. The operator $\boldsymbol{\Omega}$ is defined by

$$\boldsymbol{\Omega}(\boldsymbol{\omega}) = \begin{bmatrix} 0 & -\boldsymbol{\omega}^T \\ \boldsymbol{\omega} & -\lfloor \boldsymbol{\omega} \times \rfloor \end{bmatrix}, \tag{9}$$

$$\text{where } \lfloor \boldsymbol{\omega} \times \rfloor = \begin{bmatrix} 0 & -\omega_z & \omega_y \\ \omega_z & 0 & -\omega_x \\ -\omega_y & \omega_x & 0 \end{bmatrix}. \tag{10}$$

The state estimate and error covariance matrix are propagated at IMU rate using [12] and [13]. We highlight that this is a first-order numerical integrator based on our existing implementation. Higher-order numerical integration [14] would limit error growth during the IMU-only navigation phase but was considered beyond the scope of this project. Equations 8 show that Titan's rotation is not modeled in the system. This was deemed to be a reasonable assumption given Titan's slow rotation and the overall EDL duration. Within this assumption, the $\{PCI\}$ is equivalent to a terrain-fixed frame. The gravity vector $\boldsymbol{g}$ was computed using Newton's point-mass equation.

Map Matching Visual Update

Map matching refers to the registration of the descent image onto a map stored in the spacecraft's on-board computer memory. This map is constructed apriori from orbital orthoimage and elevation data. Map matching for Titan EDL is investigated in our companion paper [15]. Our state estimator assumes it is being provided the 3D coordinates of the center of the matched descent image in the $\{PCI\}$ frame. This is equivalent to a 1-landmark minimal point update. Map matching may be able to provide stronger constraints, but the authors decided to stick to a conservative design at this point given the low quality of orbital data available at Titan.

The mapped landmark visual measurement is the pinhole projection of $\boldsymbol{p}_j$ over the normalized image plane $f = 1$ of camera frame $\{c_i\}$ at time i of the terrain landmark backprojected from the center of the image

$${}^i\boldsymbol{z}_m = \frac{1}{{}_{c_i}z_m} \begin{bmatrix} {}_{c_i}x_m \\ {}_{c_i}y_m \end{bmatrix} + \boldsymbol{n}_m \tag{11}$$

where the cartesian coordinates of the mapped landmark $\boldsymbol{p}_m$ in camera frame $\{c_i\}$ can be related to the map coordinates in $\{PCI\}$ by

$${}_{c_i}\boldsymbol{p}_m = \begin{bmatrix} {}_{c_i}x_m & {}_{c_i}y_m & {}_{c_i}z_m \end{bmatrix}^T \tag{12}$$

$$= \boldsymbol{C}(\boldsymbol{q}^{c_i}_{PCI}) \left(\begin{bmatrix} {}_{PCI}x_m \\ {}_{PCI}y_m \\ {}_{PCI}z_m \end{bmatrix} - \boldsymbol{p}^{c_i}_{PCI} \right), \tag{13}$$

and $\boldsymbol{n}_m$ is a zero-mean white Gaussian feature measurement noise, for which the covariance matrix is derived from [15].

Authorized licensed use limited to: Jet Propulsion Laboratory. Downloaded on November 18,2024 at 21:16:46 UTC from IEEE Xplore. Restrictions apply.

Feature Tracking Visual Update

The vision states are additional filter states necessary to process unmapped image feature tracks in *Simultaneous Localization And Mapping* (SLAM) fashion. These states

$$\boldsymbol{x}_V = \begin{bmatrix} {\boldsymbol{p}_{PCI}^{c_1}}^T & \cdots & {\boldsymbol{p}_{PCI}^{c_M}}^T & {\boldsymbol{q}_{PCI}^{c_1}}^T & \cdots & {\boldsymbol{q}_{PCI}^{c_M}}^T \\ & & & \boldsymbol{f}_1^T & \cdots & \boldsymbol{f}_N^T \end{bmatrix}^T \tag{14}$$

include the orientations $\{\boldsymbol{q}_{PCI}^{c_i}\}_i$ and positions $\{\boldsymbol{p}_{PCI}^{c_i}\}_i$ of the camera frame with respect to $\{PCI\}$ at the last M image time instances, along with the 3D coordinates of N features $\{\boldsymbol{f}_j\}_j$. Each feature state $\boldsymbol{f}_j = [\alpha_j \quad \beta_j \quad \rho_j]^T$ represents the inverse-depth parametrization of terrain feature $\boldsymbol{p}_j$ with respect to an anchor pose $\{c_{i_j}\}$ selected from the sliding window of pose states. The initial inverse-depth probability distributed is centered on the inverse terrain height estimate when the feature is observed for the first time.

A feature tracking visual measurement is the pinhole projection of $\boldsymbol{p}_j$ over the normalized image plane $f = 1$ of camera frame $\{c_i\}$ at time i

$${}^i\boldsymbol{z}_{v,j} = \frac{1}{{}^{c_i}z_j}\begin{bmatrix} {}^{c_i}x_j \\ {}^{c_i}y_j \end{bmatrix} + \boldsymbol{n}_v \tag{15}$$

where the cartesian coordinates of feature $\boldsymbol{p}_j$ in camera frame $\{c_i\}$ are related to its inverse-depth parameters in anchor frame $\{c_{i_j}\}$ through

$${}^{c_i}\boldsymbol{p}_j = [{}^{c_i}x_j \quad {}^{c_i}y_j \quad {}^{c_i}z_j]^T \tag{16}$$

$$= \boldsymbol{C}(\boldsymbol{q}_{PCI}^{c_i})\left(\boldsymbol{p}_{PCI}^{c_{i_j}} + \frac{1}{\rho_j}\boldsymbol{C}(\boldsymbol{q}_{PCI}^{c_{i_j}})^T\begin{bmatrix}\alpha_j \\ \beta_j \\ 1\end{bmatrix} - \boldsymbol{p}_{PCI}^{c_i}\right), \tag{17}$$

and ${}^i\boldsymbol{n}_v$ is a zero-mean white Gaussian feature measurement noise, which is derived from our companion paper [15].

Additional implementation details can be found in our previous work [6, 7].

5. Monte Carlo Simulation Results

To evaluate TRN state estimation performance, a Monte Carlo simulation was developed for the Maracaibo Lacus scenario using a Titan direct entry. The initial epoch of the simulation begins at E-10 min. The sequence of events in the simulation encompasses a simplified form of the full ConOps described in Figures 3 and 4. A full entry sequence for a capsule with zero spin rate is considered. Inertial propagation of the IMU begins at E-10 min. The drogue parachute is deployed following peak deceleration at approximately 150 km altitude. Heatshield separation and other parachute deployments were ignored. At 41 km altitude, the parafoil is deployed and the VIO phase begins at 40 km. The VIO phase uses map matching from 40 km to 20 km altitude. Feature tracking is used from 20 km altitude to ground. During the VIO phase, the parafoil system follows a straight line flight for the remainder of the descent to the ground with a 1.9 glide ratio.

Monte Carlo simulations were executed for a total of 500 trials that included two different map matching schemes. Two types of map matching updates were considered. The first scheme uses a single landmark while the second scheme uses four landmarks to accomplish map matching. While the 4-landmark case obviously provides more information about the pose, it may prove challenging to match more than 1 landmark with existing terrain maps in the difficult Titan conditions, as discussed in our companion paper [15]. The initial truth and navigation states for each trial at E-10 min were calculated with the error statistics shown in Figure 12. State estimation results are presented in terms of Root Sum

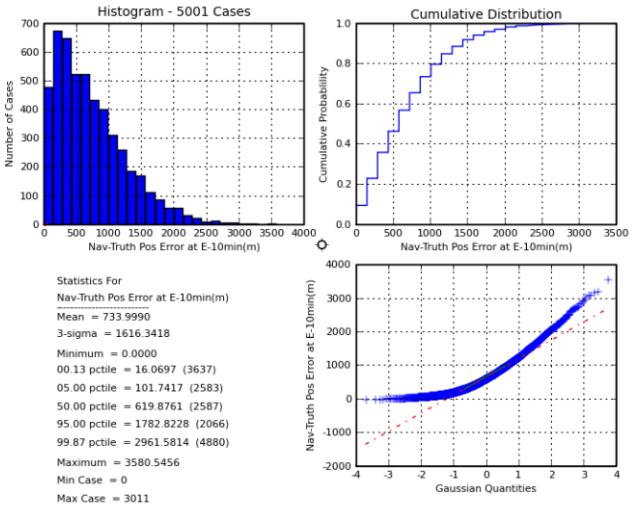

Figure 12. Initial state error statistics for EFPA -51°.

Square (RSS) position and attitude determination error and standard deviation across all of the Monte Carlo trials. The results are split into an IMU-only phase and a VIO phase. The IMU-only phase begins at E-10 min and ends at parafoil deployment. This is followed by the VIO phase, which ends at touchdown. The duration of the IMU-only phase is approximately 2470 sec while the VIO phase duration is approximately 6105 sec. Figures 13 and 14 show the position

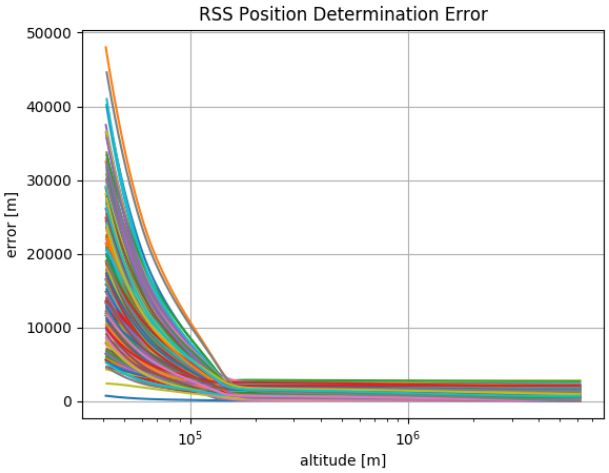

Figure 13. RSS of the position determination error for each trial as a function of altitude during IMU-only phase.

and attitude determination errors as a function of altitude for each of the trials. During this phase, inertial propagation is

Authorized licensed use limited to: Jet Propulsion Laboratory. Downloaded on November 18,2024 at 21:16:46 UTC from IEEE Xplore. Restrictions apply.

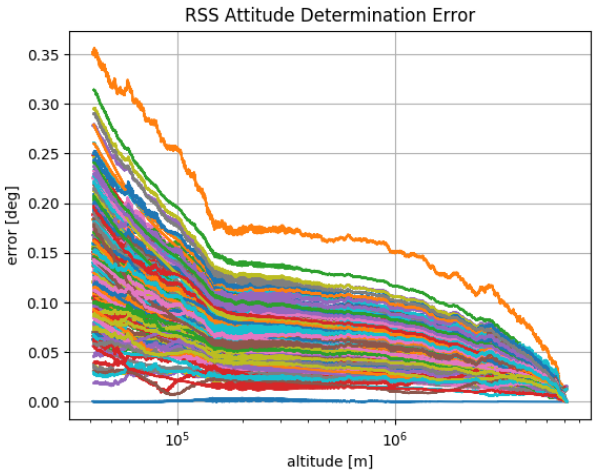

Figure 14. RSS of the attitude determination error for each trial as a function of altitude during IMU-only phase.

based on IMU-only. Also, the constant (turn-on) gyro rate bias is uncorrected at the beginning of the simulation. Error growth is expected during this dead-reckoning phase due to the lack of any state updates. Note that the error drift rate increases at 150 km due to aerodynamic disturbances at peak deceleration. Two of the trials were selected as bounding cases that included a case with no sensor errors (blue) and a case with all sensor errors set to 3-σ (orange) values. These cases are clearly seen as lower and upper bounds in Figures 13 and 14. Figures 15 and 16 show the resulting standard

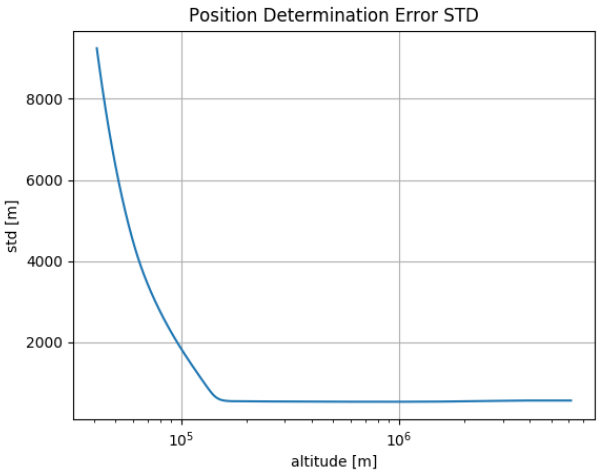

Figure 15. Standard deviation over all trials of the RSS position determination errors during IMU-only phase.

deviation over all of the trials.

Visual processing is initiated after parafoil deployment at 40 km altitude. This includes map matching updates only. At 20 km altitude, state estimation relies solely on feature tracking updates. Figures 17 and 18 illustrate the large correction between 40 km and 20 km altitude of the error accumulated in the IMU-only phase for the 1-landmark case. The errors reduce as expected during the map matching phase since we get a pose fixed with respect to the map. Errors increase

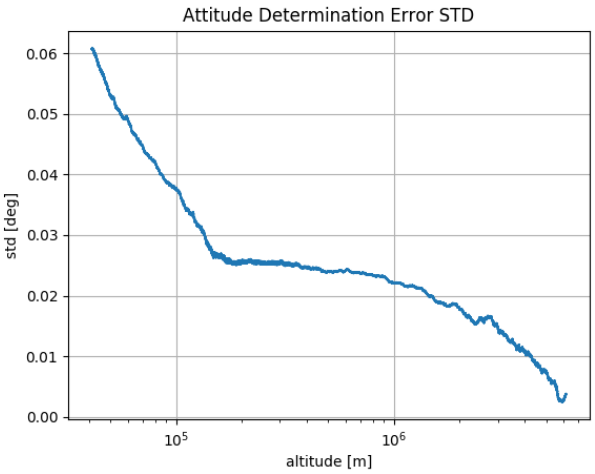

Figure 16. Standard deviation over all trials of the RSS attitude determination errors during IMU-only phase.

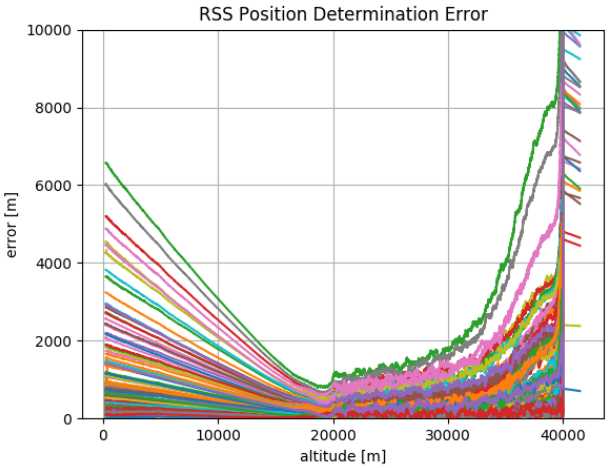

Figure 17. RSS of the position determination error for each trial as a function of altitude during VIO phase using 1 landmark for map matching.

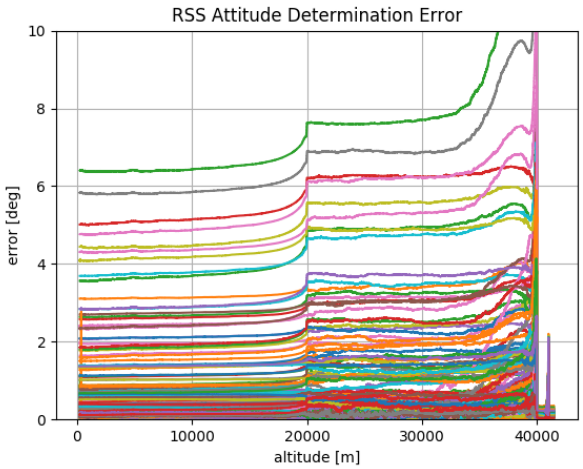

Figure 18. RSS of the attitude determination error for each trial as a function of altitude during VIO phase using 1 landmark for map matching.

Authorized licensed use limited to: Jet Propulsion Laboratory. Downloaded on November 18,2024 at 21:16:46 UTC from IEEE Xplore. Restrictions apply.

during the feature tracking phase between 20 km altitude and the ground since feature tracking is subject to drift as unmapped features enter and leave the field of view. Figures 19 and 20 show the standard deviation of position and attitude

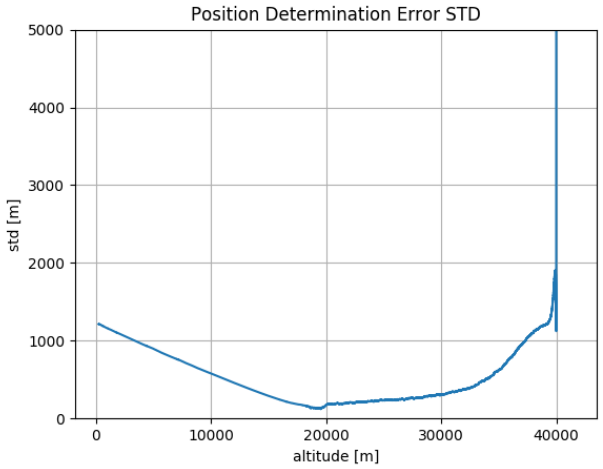

Figure 19. Standard deviation over all trials of the position determination errors during VIO phase using 1 landmark for map matching.

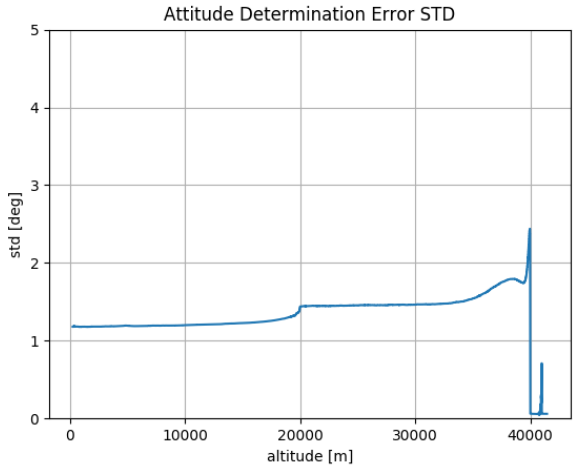

Figure 20. Standard deviation over all trials of the attitude determination errors during VIO phase using 1 landmark for map matching.

determination error during both map matching and feature tracking phases. Dispersion (in terms of standard deviation) at touchdown for 1-landmark map matching is approximately 1200 m standard deviation in position and approximately 1.2° standard deviation in attitude. It is interesting to note on Figure 18, that an attitude error is introduced by the estimator at the start of map matching and mostly remains uncorrected. We found that this error appeared in the horizontal heading, which is not constrained in the 1-landmark case, and not observable during feature tracking. The introduction of that error was imputed to the non-linearities at start of filter updates, when errors and their variances are very large and stress the EKF linearization.

Figures 21 and 22 illustrate VIO phase performance using

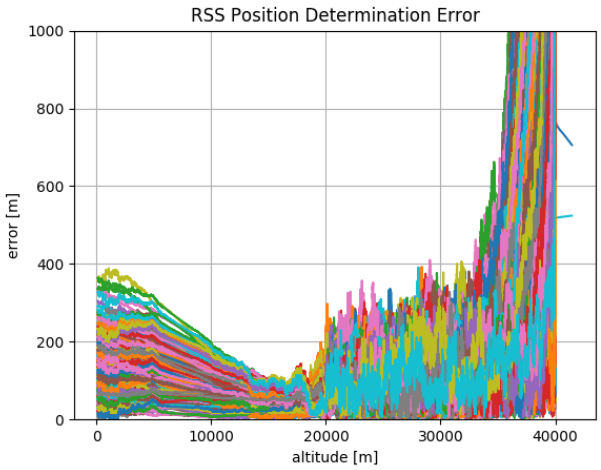

Figure 21. RSS of the position determination error for each trial as a function of altitude during VIO phase using 4 landmarks for map matching.

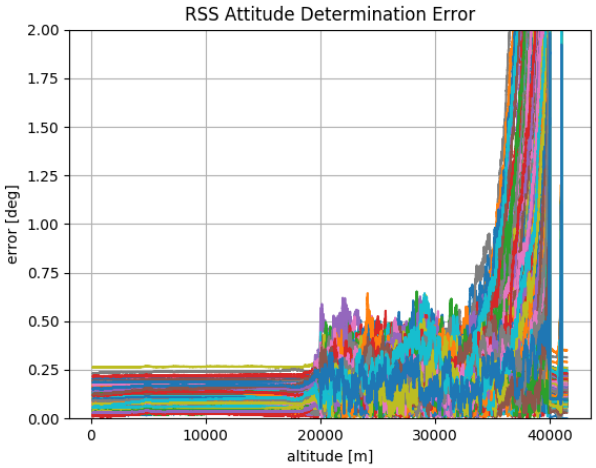

Figure 22. RSS of the attitude determination error for each trial as a function of altitude during VIO phase using 4 landmarks for map matching.

4-landmark map matching. Dispersion at touchdown with four landmarks is 100 m in position, and under 0.1° in attitude. The better performance of the 4-landmark case is not surprising given the information. In particular and unlike in the 1-landmark case, the full pose is now observable during the map matching , including the horizontal heading. As can be seen in Figure 22, although errors are still introduced due to non-linearites at the beginning of map matching, they are then observed and corrected. We can conclude that multiple landmark matching is a key performance driver, improving accuracy by one order of magnitude.

6. Summary and Future Work

In this paper, a Titan mission design and corresponding EDL architecture was discussed. A complete Titan EDL ConOps was developed for a 45° spherecone aeroshell. This included entry phase, parachute phase, and descent and landing phases where a guided parafoil is used in conjuction with TRN

Authorized licensed use limited to: Jet Propulsion Laboratory. Downloaded on November 18,2024 at 21:16:46 UTC from IEEE Xplore. Restrictions apply.

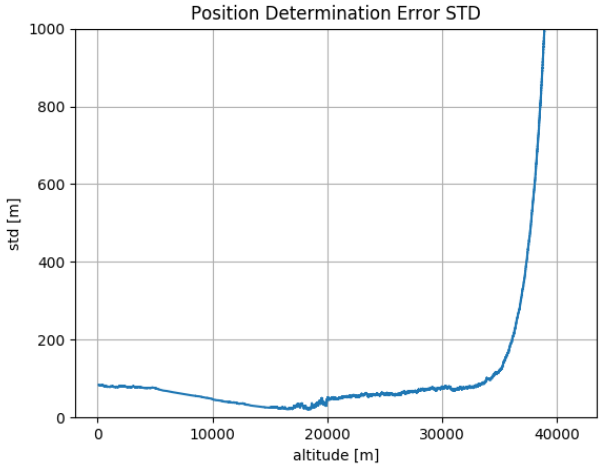

Figure 23. Standard deviation over all trials of the position determination errors during VIO phase using 4 landmarks for map matching.

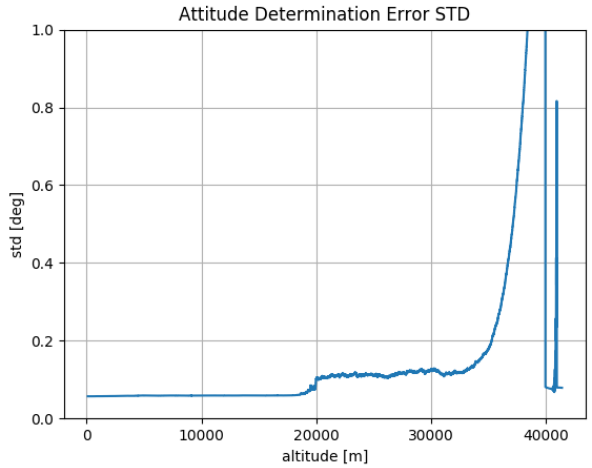

Figure 24. Standard deviation over all trials of the attitude determination errors during VIO phase using 4 landmarks for map matching.

state estimation. An integrated end-to-end simulation was constructed using the DSENDS multi-mission simulation framework to handle the capsule and parafoil dynamics, sensor modeling, ROS interface for state estimation, and Monte Carlo analysis. The simulation framework is available for future Titan precision landing studies with different design points. The results of the Monte Carlo analysis revealed 90 m standard deviation in position determination error and 0.1° standard deviation in attitude determination error at touchdown using 4 landmarks for VIO map matching.

Future work includes evaluation of motion planning and closed-loop control with TRN state estimation. Several improvements can also be made to the state estimation algorithm, which include higher order integration, an improved altimeter model to vary terrain range measurements as a function of the parafoil attitude, and accounting for Titan rotation and non-spherical surface model.

REFERENCES

[1] Folkner, W. M., et al. "Winds on Titan from ground based tracking of the Huygens probe." Journal of Geophysical Research: Planets 111.E7 (2006).

[2] Quadrelli, M. B. (2005), A Novel Approach to Planetary Precision Landing using Parafoils, Advances in the Astronautical Sciences 120, 229-244.

[3] Yakimenko, Oleg A. "Precision Aerial Delivery Systems: Modeling, Dynamics, and Control" AIAA, Volume 248 Progress in Astronautics and Aeronautics, 2015.

[4] Quadrelli, M., Schutte, A., Rimani, J., and Ermolli, L.: "Aero Maneuvering Dynamics and Control for Precision Landing on Titan" IEEE Aerospace Conference, 2019.

[5] https://dartslab.jpl.nasa.gov

[6] Delaune, J., Hewitt, R., Lytle, D., Sorice, C., Thakker, R., and Matthies, L: "Thermal-Inertial Odometry for Autonomous Flight Throughout the Night" IEEE IROS 2019.

[7] J. Delaune and D. Bayard, "xVIO: Visual-inertial odometry implementation," Jet Propulsion Laboratory (available upon request), Tech. Rep., 2019.

[8] Cameron, J., Jain, J., Burkhart, D., Bailey, E., Balaram, B., Bonfiglio, E., Grip, H., Ivanov, M., and Sklyanskiy, E.: "DSENDS: Multi-mission Flight Dynamics Simulator for NASA Missions" AIAA SPACE Conference and Exposition, 2016.

[9] Yelle, R., Strobell, D., Lellouch, E., and Gaultier D.: "Engineering Models for Titan's Atmosphere" Huygens: Science, Payload and Mission, Proceedings of an ESA conference, pg. 243, 1997.

[10] Hayes, A.G., "The Lakes and Seas of Titan", Annual Review of Earth and Planetary Sciences, vol. 44, p.57-83, 2016.

[11] https://naif.jpl.nasa.gov/naif/toolkit.html

[12] S. Weiss and R. Siegwart, "Real-time metric state estimation for modular vision-inertial systems," in International Conference on Robotics and Automation (ICRA). IEEE, 2012.

[13] N. Trawny and S. Roumeliotis, "Indirect kalman filter for 3d attitude estimation," University of Minnesota, Tech. Rep., 2005.

[14] A. I. Mourikis and S. I. Roumeliotis. A multi-state constraint Kalman filter for vision-aided inertial navigation. In Proceedings of the IEEE International Conference on Robotics and Automation (ICRA), pages 3565–3572, 2007.

[15] L. Matthies, S. Daftry, B. Rothrock, A. Davis, R. Hewitt, E. Sklyanskiy, J. Delaune, A. Schutte and M. Malaska. Terrain Relative Navigation for Guided Descent on Titan. Submitted to the IEEE Aerospace conferece, 2019.

[16] P. Couzin and A.M. Schipper. Huygens Mission Post Flight Engineering Analysis. Alcatel, 2006.

Authorized licensed use limited to: Jet Propulsion Laboratory. Downloaded on November 18,2024 at 21:16:46 UTC from IEEE Xplore. Restrictions apply.

BIOGRAPHY

Aaron Schutte *is a Robotics Systems Engineer in the Modeling and Simulation Group at NASA JPL where he supports the development of advanced high-fidelity multi-mission simulation tools in the DARTS Lab. Prior to joining JPL he worked as a researcher in the Vehicle Systems Division at The Aerospace Corporation developing computational tools and algorithms for analysis of spacecraft GN&C systems and GPS. His primary contributions are in the development of high fidelity rigid and flexible multibody simulations, spacecraft control design and estimation techniques, and development of automatic derivative methods. He obtained his Ph.D. from University of Southern California in 2009. He is a Senior Member of the AIAA and has served as a regular member of the AIAA GN&C Technical Committee.*

Jeff Delaune *received his Ph.D. in Robotics from Institut Supérieur de l'Aéronautique et de l'Espace (ISAE, France) in 2013, after a M.S. in Astronautics and Space Engineering from Cranfield University (United Kingdom), and a B.S./M.S. in Engineering from École Centrale de Nantes (France). He is currently a robotics technologist at the Jet Propulsion Laboratory. He develops autonomous navigation systems for planetary exploration, with a focus on flying vehicles. Jeff was part of the navigation team for NASA's Mars Helicopter flight project. His interests include state estimation, sensor fusion, perception and computer vision.*

Evgeniy Sklyanskiy *received a B.S. in Aerospace Engineering from University of Illinois at Urbana-Champaign (UIUC). He continued the graduate studies at UIUC, and acquired a M.S. in Applied Mathematics and Aerospace Engineering. In the year of 2004, Evgeniy joined JPL and was working on low thrust trajectory optimization problems in the Mission Design and Navigation (MDNAV) section under the Outer Planetary group. Later in the career, the author has joined the EDL Guidance and Control Systems Group, where he has worked on Hayabusa/MUSES-C comet sample return mission, MSL surface operations and InSight MDNAV/EDL targeting analysis.*

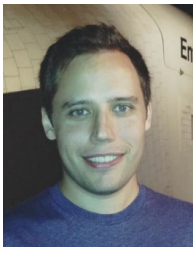

Robert Hewitt *received his Ph.D. degree in Electrical and Computer Engineering in 2018 from Queen's University (Kingston, Canada), after a M.A.Sc. in Aerospace Engienering from Carleton University (Ottawa, Canada) and a B.A.Sc in Engineering Physics from the University of Saskatchewan (Saskatoon, Canada). He is currently a post-doctoral research scientist at the Jet Propulsion Laboratory. He develops autonomous navigation systems for aerial and ground vehicles used in prospective planetary missions. His interests include state estimation, perception, and instrumentation.*

Shreyansh Daftry *is a Robotics Technologist at NASA Jet Propulsion Laboratory, California Institute of Technology. He received his M.S. degree in Robotics from Carnegie Mellon University, and his B.S. degree in Electronics and Communication Engineering in 2013. His research interests lies at the intersection of space technology and autonomous robotic systems, with an emphasis on computer vision and machine learning. At JPL, he works on mission formulation for Mars Sample Return, and technology development for autonomous navigation of ground, airborne and subterranean robots.*

Marco Quadrelli *is an internationally renowned expert in modeling for dynamics and control of complex space systems. He has a Masters Degree in Aeronautics and Astronautics from MIT and a PhD in Aerospace Engineering from Georgia Tech. He was a visiting scientist at the Harvard-Smithsonian Center for Astrophysics, and a lecturer at the Caltech Graduate Aeronautical Laboratories. After joining NASA JPL in 1997 he has contributed to a number of flight projects including the Cassini---Huygens Probe, Deep Space One, the Mars Aerobot Test Program, the Mars Exploration Rovers, the Space Interferometry Mission, the Autonomous Rendezvous Experiment, and the Mars Science Laboratory, among others. He has been the Attitude Control lead of the Jupiter Icy Moons Orbiter Project, and the Integrated Modeling Task Manager for the Laser Interferometer Space Antenna. He has led or participated in several independent research and development projects in the areas of computational micromechanics, dynamics and control of tethered space systems, formation flying, inflatable apertures, hypersonic entry, precision landing, flexible multibody dynamics, guidance, navigation and control of spacecraft swarms, terramechanics, and precision pointing for optical systems. He is an Associate Fellow of the American Institute of Aeronautics and Astronautics, a NASA Institute of Advanced Concepts Fellow, and a Caltech/Keck Institute for Space Studies Fellow.*

Larry Matthies *is a Senior Research Scientist at the Jet Propulsion Laboratory. He has conducted research there on computer vision-based autonomous navigation of robotic vehicles for 30 years. He defined initial versions of several vision algorithms that have been used on Mars or are their way to Mars for the 2020 mission, including stereo vision and visual odometry for rover navigation, feature tracking for velocity estimation during terminal descent in the Descent Image Motion Estimation System for the MER mission, and terrain relative navigation for Mars precision landing, which is now built into the 2020 Mars landing system. He has also been a Principal Investigator in many autonomous navigation research programs funded by DARPA and the U.S. Army. He obtained his PhD in computer science from Carnegie Mellon University in 1989 and is a Fellow of the IEEE.*

Authorized licensed use limited to: Jet Propulsion Laboratory. Downloaded on November 18,2024 at 21:16:46 UTC from IEEE Xplore. Restrictions apply.